All-Optical Blister Test of Suspended Graphene Using Micro-Raman Spectroscopy

Dominik Metten, François Federspiel, Michelangelo Romeo, and Stéphane Berciaud*

Institut de Physique et Chimie des Matériaux de Strasbourg and NIE, UMR 7504, Université de Strasbourg and CNRS, 23 rue du Læss, BP43, 67034 Strasbourg Cedex 2, France

(Received 11 July 2014; published 11 November 2014)

We report a comprehensive micro-Raman study of a pressurized suspended graphene membrane that hermetically seals a circular pit, etched in a Si/SiO_2 substrate. Placing the sample under a uniform pressure load results in bulging of the graphene membrane and subsequent softening of the main Raman features, due to tensile strain. In such a microcavity, the intensity of the Raman features depends very sensitively on the distance between the graphene membrane and the Si substrate, which acts as the bottom mirror of the cavity. Thus, a spatially resolved analysis of the intensity of the *G*- and 2*D*-mode features as a function of the pressure load permits a direct reconstruction of the blister profile. An average strain is then deduced at each pressure load, and Grüneisen parameters of 1.8 ± 0.2 and 2.4 ± 0.2 are determined for the Raman *G* and 2*D* modes, respectively. In addition, the measured blister height is proportional to the cubic root of the pressure load, as predicted theoretically. The validation of this scaling provides a direct and accurate determination of the Young's modulus of graphene with a purely optical, hence contactless and minimally invasive, approach. We find a Young's modulus of (1.05 ± 0.10) TPa for monolayer graphene, in a perfect match with previous nanoindentation measurements. This all-optical methodology opens avenues for pressure sensing using graphene and could readily be adapted to other emerging two-dimensional materials and to nanoresonators.

DOI: 10.1103/PhysRevApplied.2.054008

I. INTRODUCTION

Two-dimensional crystals [1], being just one or a few atoms thick and having lateral dimensions ranging from micrometers up to macroscopic scales, are a new class of solid-state membranes. Among these systems, graphene has attracted considerable interest, due to its unique electronic band structure [2] as well as its outstanding materials properties. In particular, graphene is endowed with exceptional mechanical properties, such as a large Young's modulus and intrinsic strength [3], ultrastrong adhesion [4], and impermeability to standard gases [5]. Owing to the great electrical controllability of graphene [6], suspended graphene membranes can conveniently be integrated into nanoelectromechanical resonators [7,8]. In addition, graphene interacts strongly with optical radiation [9]. However, being atomically thin, a single layer of graphene is quasitransparent over the infrared and visible ranges [10,11]. These features allow the optical readout of mechanical resonances [5,7,12,13] and open perspectives for optomechanical studies [14].

It was also recently demonstrated that the impermeability and ultrastrong adhesion of graphene make it possible to form blisters (or balloons), by applying a pressure difference between both sides of a suspended graphene membrane [5]. Such systems are highly promising for molecular sieving applications [15]. In practice, bulging of the atomically thin membrane can be quantitatively investigated by using atomic force microscopy (AFM) [4,5] or nanoindentation [3], in what is known as a blister (or bulge) test [16]. In addition, the resulting strain field in the bulged graphene membrane may be probed optically, through frequency shifts of the main Raman scattering features [17–20]. A quantitative analysis requires, however, knowledge of the Grüneisen parameters, whose determination is challenging in pressurized suspended graphene membranes.

Here, we show that micro-Raman scattering alone not only permits one to investigate strain-induced phonon softening in pressurized graphene membranes, but also readily provides the blister topography, resulting in a comprehensive, all-optical blister test. The height profile of a pressurized graphene blister is determined from the analysis of the integrated intensity of the main (*G* and 2*D*) Raman scattering features of graphene. This analysis allows a direct determination of the tensile strain. The softening of the Raman features is then examined under the known tensile strain, as a function of the pressure load. The Grüneisen parameters for the *G*- and 2*D*-mode features and, importantly, the Young's modulus of graphene are then obtained only by optical means. This approach is contactless and can thus be applied in a large variety of experimental conditions. It could serve as a guide for further optical and optomechanical studies on graphene and related systems.

*stephane.berciaud@ipcms.unistra.fr

II. EXPERIMENTAL METHODS

For an accurate blister test, high-quality, impermeable, and defect-free graphene is mandatory. We therefore prepare our graphene samples by mechanical exfoliation of natural graphite. This material is known to be well suited to the investigation of the intrinsic properties of graphene. Graphene layers are deposited over circular pits that have been patterned in a Si/SiO_2 substrate by optical lithography, followed by reactive ion etching and careful drying, in order to eliminate liquid residues inside the pits [21]. No silicon oxide is left within the pits. The mechanically exfoliated graphene layers are tightly clamped around the border of the pit by van der Waals forces, resulting in a hermetically sealed drum, in which a constant number of air molecules is trapped. The typical pit radius is $a \approx 4\ \mu$m, and the pit depth h_0 is measured with a profilometer. In the following, we present results obtained for a sample with $h_0 = (395 \pm 10)$ nm. Similar results are obtained on two other samples with different pit depths (see Supplemental Material [22]).

As a characterization tool, we make use of micro-Raman scattering spectroscopy [23,24], which is highly sensitive to the number of layers, disorder [25,26], doping, and, importantly, strain [18–20,27–34]. Since suspended graphene is immune to substrate-induced doping [21,35] and minimally sensitive to atmospheric doping [36], these samples allow the direct investigation of strain-induced changes in the Raman spectrum of graphene, without spurious contributions from a residual charge-carrier density [37]. Here, micro-Raman measurements are performed in a backscattering geometry, with a homebuilt setup, by using a 20 × objective (N.A. = 0.45) and a 532-nm laser beam focused onto an approximately 1.2-μm (full width at half maximum) spot. The objective is mounted onto a piezoelectric stage allowing spatially resolved Raman studies. The collected Raman scattered light is dispersed onto a charge-coupled device array by a single-pass optical spectrometer, with a spectral resolution better than 2 cm^{-1}. The laser beam is linearly polarized, and the laser power is maintained at 0.7 mW, in order to avoid laser-induced local heating and subsequent thermally induced spectral shifts or line-shape changes of the Raman features [38]. Suspended graphene monolayers are unambiguously identified from the characteristic line shape of their Raman 2*D*-mode feature [35], and their undoped character is systematically confirmed from a detailed spatially resolved Raman study [21]. The relative integrated intensity of the defect-related *D* mode to that of the *G* mode is less than 1% on the samples investigated here. In order to form graphene blisters, the samples are held in a vacuum chamber equipped with a quartz window for optical access. The external pressure p_{ext} is smoothly varied from approximately 10^{-2} Pa to atmospheric pressure (100 ± 2) kPa. Considering the bulging of the graphene membrane, we estimate, by using the ideal gas law, that the corresponding pressure load $\Delta p = p_{int} - p_{ext}$, i.e., the difference between pressures inside and outside the blister, varies between (0 ± 2) and (74 ± 5) kPa, respectively. More details on the determination of Δp are given in Supplemental Material [22]. Importantly, the highest Δp achieved here is more than one order of magnitude below the threshold, at which delamination occurs [4]. Consequently, we consider a constant blister radius throughout this article.

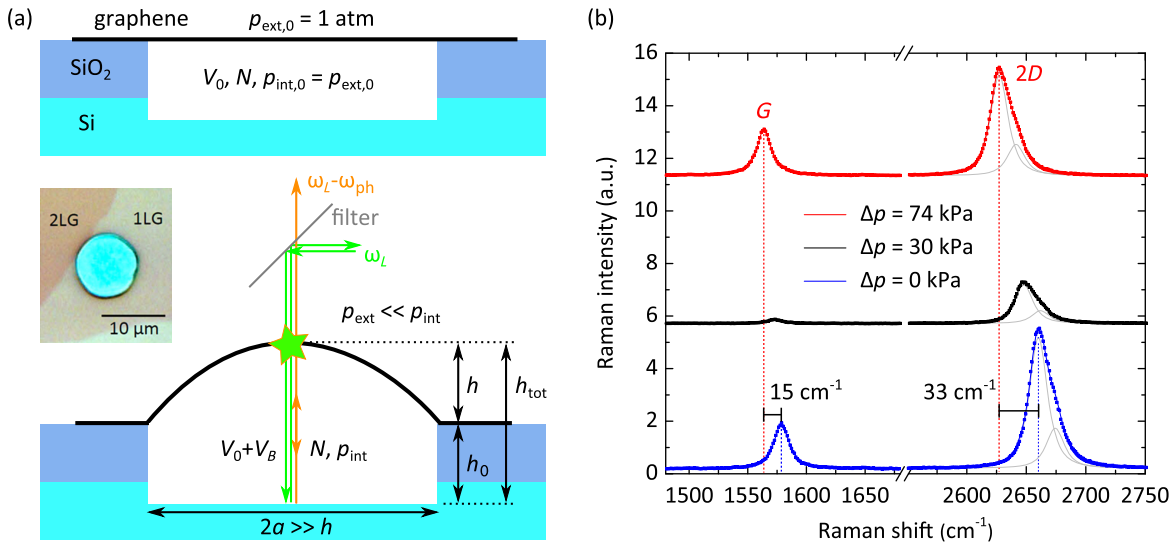

FIG. 1. Formation of a pressurized graphene blister. (a) Sketch of a suspended graphene membrane at pressure equilibrium (upper part) and under a uniform pressure load (lower part). An optical image of a suspended graphene monolayer sealing a cylindrical pit with a radius $a \approx 4\ \mu$m is shown in the center left part of (a). (b) Micro-Raman spectra recorded at the center of the graphene membrane at different values of $\Delta p = p_{int} - p_{ext}$.

Figure 1 shows a schematic of our experimental approach. The volume of the cylindrical pit is V_0, V_B denotes the volume of the blister, and N is the number of trapped air molecules. We note $h(r) \ll a$, the vertical displacement of the graphene layer, and $h_{\mathrm{tot}}(r)$, the total distance between graphene and the underlying Si substrate, at a distance r from the center of the blister. The maximum deflection $h(0)$ is denoted h_{max}. Considering our sample geometry, we estimate an upper bound for the maximum angle between the substrate and the bulged graphene of approximately 0.1 rad. Therefore, we assume that the laser beam always impinges on the graphene membrane at quasinormal incidence.

Over long time scales, on the order of several hours, graphene blisters tend to deflate, essentially due to slow diffusion of air molecules through the Si/SiO_2 substrate [4,5]. In order to verify whether the leak rate has to be considered, Raman measurements are performed on suspended graphene membranes at $p_{\mathrm{ext}} = p_{\mathrm{int}} = 100$ kPa before pumping out the vacuum chamber and again at $p_{\mathrm{ext}} = 100$ kPa, after a series of measurements as a function of p_{ext}, starting from $p_{\mathrm{ext}} \approx 10^{-2}$ Pa. No significant changes of the Raman frequencies or of the integrated intensity of the Raman features are observed, which demonstrates that the leak rate of our pressurized membrane could be neglected over the duration of a measurement run. Consequently, a constant N is assumed in the analysis described below. Data performed on longer time scales, revealing for a finite leak rate, evidenced by the development of a concave blister profile at the end of a measurement cycle, are shown in Supplemental Material [22].

III. STRAIN-INDUCED PHONON SOFTENING

Raman spectra recorded at the center of the membrane for $\Delta p = 0$ kPa and $\Delta p = 74$ kPa are shown in Fig. 1(b). At pressure equilibrium, the Raman G-mode feature (fit to a single Lorentzian) is centered at $\omega_G = 1578.8$ cm^{-1}, with a full width at half maximum (FWHM) of $\Gamma_G = (15 \pm 0.5)$ cm^{-1}, characteristic of an undoped sample [21]. Its integrated intensity is denoted I_G. We note that Γ_G remains at (15 ± 0.5) cm^{-1} over the suspended membrane at each value of Δp. This value confirms that doping from the surrounding air molecules can be neglected and that suspended graphene membranes allow investigations of strain without parasitic effects from unintentional doping. The $2D$-mode feature shows an asymmetric line shape, as typically observed on suspended graphene, and is fit to a modified double Lorentzian profile, as in Ref. [35]. The lower-energy feature has a much higher integrated intensity, and its peak frequency coincides with the peak frequency of the $2D$-mode feature. The spectral shift between the low- and the high-energy features (approximately 15 cm^{-1}), as well as their integrated intensity ratio (approximately 3), is also constant over the suspended part, irrespective of Δp. Hence, we use the position of the low-energy $2D$-mode subfeature as the peak frequency, denoted ω_{2D}, and the sum of the integrated intensities of both subfeatures is referred to as I_{2D}. The fact that values of $\omega_G = 1578.8$ cm^{-1} and $\omega_{2D} = 2660.0$ cm^{-1} are slightly lower than expected for pristine graphene is attributed to an initial built-in strain of less than 0.1%, in accordance with our previous studies [37]. Very similar results to those described below are also obtained on suspended samples, on which no significant built-in strain is observed (see Supplemental Material [22]). This similarity suggests that prestrain has no major effect on bulging under a uniform pressure load, which is consistent with the negligible bending rigidity of graphene [3,16].

When placing the sample under a high vacuum [see the red curve in Fig. 1(b)], both the G- and $2D$-mode features soften (by 15 and 33 cm^{-1} at the center of the membrane, respectively) but retain their peak shapes and show comparable values of I_G and I_{2D}. A spectrum taken at an intermediate $\Delta p = 30$ kPa is also shown. Interestingly, it reveals a striking decrease of I_G, by one order of magnitude, and of I_{2D} by a factor of only approximately 4, compared to the measurement at $\Delta p = 0$ kPa. These variations are key in our analysis and are discussed later in the manuscript. We first concentrate on the Raman shifts and their dependence on Δp and on r.

Figure 2 displays two-dimensional maps, of ω_G (a) and ω_{2D} (b), recorded at $\Delta p = 74$ kPa on the sample shown in Fig. 1(a). The pressurized suspended region exhibits centrosymmetric distributions of ω_G and ω_{2D} with minimum values much smaller than on the supported region. Indeed, a few microns away from the pit, the pressure-induced strain is relaxed, and homogeneous distributions of $\omega_G = (1581 \pm 1)$ cm^{-1}, $\omega_{2D} = (2661 \pm 2)$ cm^{-1}, and $\Gamma_G = 9.5 \pm 0.5$ cm^{-1} are observed on supported graphene. The latter value suggests that this region is slightly doped, by approximately 2×10^{12} cm^{-2}, while the values of ω_G and ω_{2D} are consistent with a built-in tensile strain comparable to the one observed on the suspended region at $\Delta p = 0$ kPa [21,31,37].

In Fig. 2(c), we further compare the G- and $2D$-mode frequencies at $\Delta p = 0$ kPa and $\Delta p = 74$ kPa along a radial line scan across the pit. For both data sets, the measured G-mode frequencies converge very near the border of the pit (at approximately 4 μm from the center), whereas for ω_{2D} the convergence is observed at approximately 5.5 μm from the center of the pit. We attribute this difference to the subtle interplay between the evolution of ω_G and ω_{2D}, due to strain relaxation at the edges of the pit, and the presence of residual doping on the supported part [31]. These effects will be discussed in detail elsewhere, since we are interested in studying pure strain on suspended graphene.

To further unveil phonon softening induced by tensile strain, we now investigate the correlation between ω_{2D} and ω_G as a function of Δp and the position on the graphene

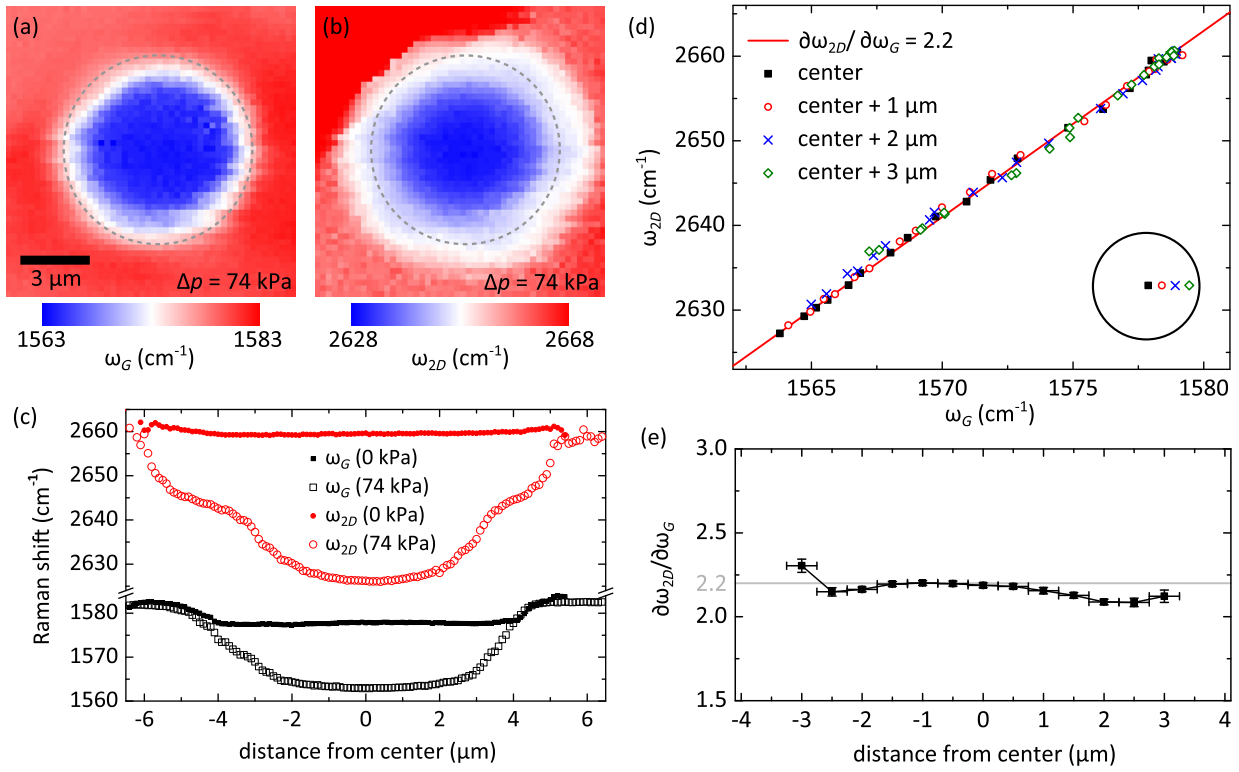

FIG. 2. Strain-induced phonon softening. (a),(b) Spatially resolved Raman maps of the G- and $2D$-mode frequencies recorded on the sample shown in Fig. 1(a), under a uniform pressure load of $\Delta p = 74$ kPa. The step size is 250 nm. The upper left part of the sample contains a supported bilayer region, where, as expected, ω_{2D} upshifts significantly. The border of the pit is represented by gray dashed circles. (c) High-resolution radial line scans of the frequencies of the G- (black squares) and $2D$-mode (red circles) features, recorded across the pit at $\Delta p = 0$ kPa (filled symbols) and $\Delta p = 74$ kPa (open symbols), with a step size of 100 nm. (d) Correlation between ω_G and ω_{2D} plotted for each pressure difference at four different values of r, ranging from $r = 0$ μm to $r = 3$ μm. The solid line is a linear fit with a slope $\partial\omega_{2D}/\partial\omega_G = 2.2$. (e) $\partial\omega_{2D}/\partial\omega_G$ as a function of r, the distance from the blister center.

membrane. For this purpose, we record Raman line scans with a step size of 500 nm for 19 different values of Δp ranging from 74 down to 0 kPa. In Fig. 2(d), we show the correlation between ω_{2D} and ω_G recorded with varying Δp, at the center of the pressurized membrane, and at $r = 1$, 2, and 3 μm from the center. At $\Delta p = 74$ kPa, ω_G (ω_{2D}) shifts down to 1563.8 cm^{-1} (2627.2 cm^{-1}) at the center, whereas ω_G (ω_{2D}) is 1567.7 cm^{-1} (2636.0 cm^{-1}) at 3 μm away from the center. As shown in Fig. 2(e), when varying Δp, the correlation between ω_{2D} and ω_G is linear, with a slope of $\frac{\partial\omega_{2D}}{\partial\omega_G} = 2.2 \pm 0.1$, irrespective of the position on the suspended graphene blister, within a distance of 3 μm from the center.

Given the membrane geometry, the pressure-induced stress and resulting tensile strain are essentially biaxial in the pressurized blister [18]. Still, there may be a dominant radial, hence uniaxial, contribution when approaching the edges of the pit [19]. In our measurements, we observe a splitting of the G-mode feature below 500 nm from the border, which may arise from uniaxial strain [27,28]. However, the resulting G-mode line shape is independent on the polarization of the incoming and scattered photons (see Supplemental Material [22]). The apparent bimodal G-mode feature is thus attributed to a superposition of the Raman responses of the supported and suspended regions, due to the finite size of the laser spot, as it has been observed by Lee, Yoon, and Cheong [19]. This result suggests that contributions from uniaxial strain cannot be unambiguously resolved in the present study. Nevertheless, uniaxial or quasiuniaxial strain presumably results in the smaller phonon softening that is observed when approaching the edges of the pressurized membrane, compared to the larger downshifts measured near the center, which arise from biaxial strain. We believe that the levels of strain achieved here are presumably too small to result in a sizable splitting of the Raman features near the edges of the graphene blister.

IV. RECONSTRUCTION OF THE BLISTER TOPOGRAPHY

We now address the strong variations of the Raman scattering intensity observed when varying Δp. Since the Si surface at the bottom of the pit acts as a semireflecting

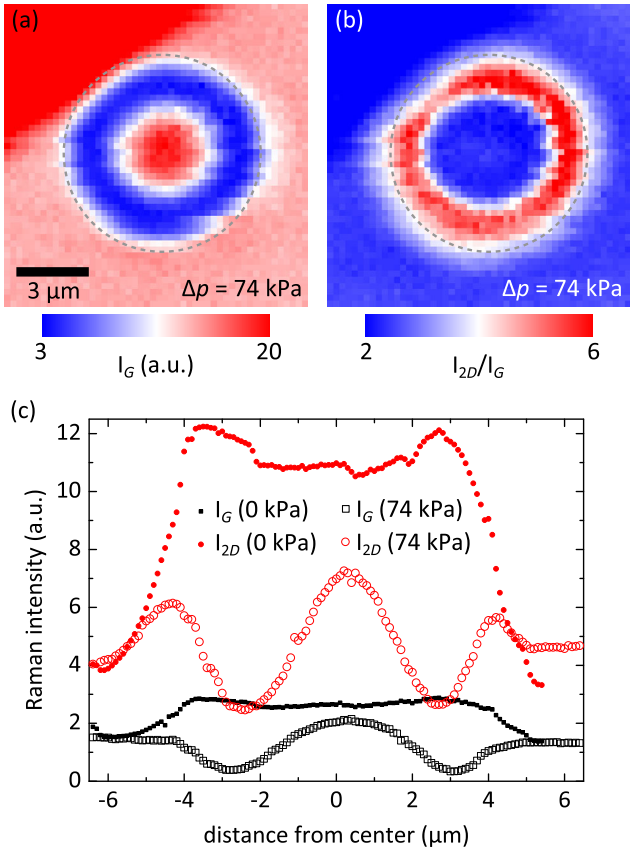

FIG. 3. Influence of the pressure load on the Raman scattering intensity. Maps of (a) the integrated intensity of the G-mode feature I_G and of (b) I_{2D}/I_G, the ratio of the integrated intensities of the $2D$- and G-mode features recorded on the sample shown in Fig. 1(a), under a uniform pressure load of $\Delta p = 74$ kPa. The step size is 250 nm. The border of the pit is represented by gray dashed circles. (c) High-resolution radial line scans of I_G (black squares) and I_{2D} (red circles), recorded across the pit at $\Delta p = 0$ kPa (filled symbols) and $\Delta p = 74$ kPa (open symbols), with a step size of 100 nm.

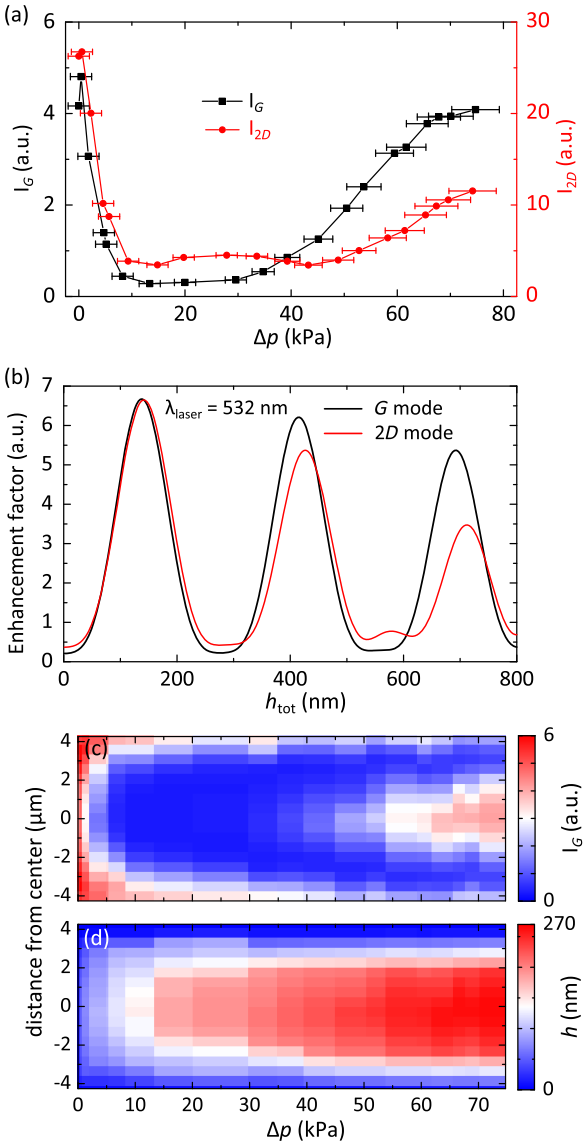

FIG. 4. Determination of the blister height from the Raman scattering intensity. (a) Evolution of the integrated intensities of the G- and $2D$-mode features measured at the center of the sample shown in Fig. 1(a), as a function of the pressure load Δp. (b) Calculated Raman enhancement factors. (c) Raman G-mode intensity I_G and (d) blister height $h(r)$, deduced from the data in (c), as a function of the distance from the blister center r and the pressure load Δp.

mirror for visible photons, we expect the intensities of the Raman G- and $2D$-mode features to depend sensitively on the height of the graphene blister, due to interference effects [39–41]. Indeed, interference rings appear clearly on the Raman maps of I_G and I_{2D}/I_G recorded at $\Delta p = 74$ kPa [see Figs. 3(a) and 3(b)]. This result demonstrates that I_G and I_{2D} vary significantly over the pressurized membrane and not in the same manner. Conversely, as shown in the line scans of the Raman scattering intensities [see Fig. 3(c)], I_G and I_{2D} are nearly constant over the suspended area at $\Delta p = 0$ kPa, which is consistent with a nearly flat suspended membrane at pressure equilibrium.

The evolution of I_G and I_{2D} as a function of Δp at $r = 0$ μm is represented in Fig. 4(a). The ratio between the maximal and minimal value of I_G (I_{2D}) reaches approximately 13 (approximately 6), and these two quantities are not proportional to each other. The Raman enhancement factor in the graphene-air-silicon layered system can be calculated with a simple analytical model, using the tabulated dielectric constants of Si and bulk graphite, as introduced by Yoon *et al.* [40]. Since we use a relatively low numerical aperture objective (N.A. = 0.45), we assume that the normal incidence approximation is valid in the vicinity of the graphene blister. The key point of this model is that the measured Raman scattering intensity depends not only on the total intensity of the laser beam (at wavelength λ_{laser}) at the location of the graphene membrane, but also on the total intensity of the

backscattered Raman G- and $2D$-mode photons at wavelengths $\lambda_{2D} > \lambda_G > \lambda_{\text{laser}}$. Both quantities are strongly dependent on h_{tot} (see Fig. 1). Consequently, I_G and I_{2D} are expected to exhibit distinct evolutions as a function of h_{tot}. Thus, from the measured Raman intensities, it is possible to deduce $h_{\text{tot}}(r)$ and, finally, the blister height $h(r) = h_{\text{tot}}(r) - h_0$.

The Raman enhancement factors for the G and $2D$ Raman modes, computed by using the analytical model of Yoon *et al.*, are shown in Fig. 4(b) as a function of h_{tot}, for $\lambda_{\text{laser}} = 532$ nm. We note that, although the values of h_{tot} corresponding to maxima and minima of the enhancement factors are essentially determined by the wavelengths of the laser and Raman scattered photons, the contrast between the maximal and minimal enhancement factors depends sensitively on materials parameters, such as the wavelength-dependent dielectric constants of Si and graphene. This contrast may also be affected by experimental factors, such as local corrugation on the Si surface, as well as slight deviations from the normal incidence approximation, arising from the numerical aperture of the microscope objective or occurring near the edges of the pressurized membrane. Consequently, the calculated enhancement factors are renormalized with respect to the experimentally measured maxima and minima of I_G and I_{2D}. In practice, this renormalization has a minor impact on the determination of $h_{\text{tot}}(r)$.

Let us emphasize that, in principle, a simple measurement of the backreflected laser intensity could be employed to deduce $h_{\text{tot}}(r)$ [13,39]. However, due to the quasitransparency of single-layer graphene, the maximum contrast expected in a reflectivity measurement is at most on the order of approximately 15% for a graphene monolayer [39], while we obtain a contrast of more than one order of magnitude on I_G. In addition, Raman measurements also provide quantitative information on the strain field in the graphene blister, as discussed above.

We now compare the data in Figs. 4(a) and 4(b). The experimental evolution of I_G and I_{2D} as a function of Δp [Fig. 4(a)] qualitatively resembles the calculated Raman enhancement factors [Fig. 4(b)]. In particular, at $\Delta p = 0$ kPa, $h_0 = (395 \pm 10)$ nm, I_G and I_{2D} are close to their maximum values, which are reached at a finite $\Delta p \approx 1$ kPa. This evolution is very consistent with the calculated enhancement factors, which predict maxima at $h_{\text{tot}} = 416$ nm ($h_{\text{tot}} = 426$ nm) for I_G (I_{2D}). Similarly, I_G and I_{2D} reach local minima at $\Delta p \approx 14$ kPa, corresponding to $h_{\text{tot}} \approx 550$ nm, and rise again towards another local maximum at higher Δp, which would correspond to $h_{\text{tot}} = 692$ nm ($h_{\text{tot}} = 712$ nm) for I_G (I_{2D}). This result readily allows us to estimate that the maximum height $h_{\text{max}} = h_{\text{tot}}(0) - h_0$ of the graphene blister, attained at $\Delta p = 74$ kPa, is close to 270 nm. Interestingly, the evolution of I_{2D} vs Δp also reveals a slight bump in the range 15–45 kPa, with a secondary maximum around

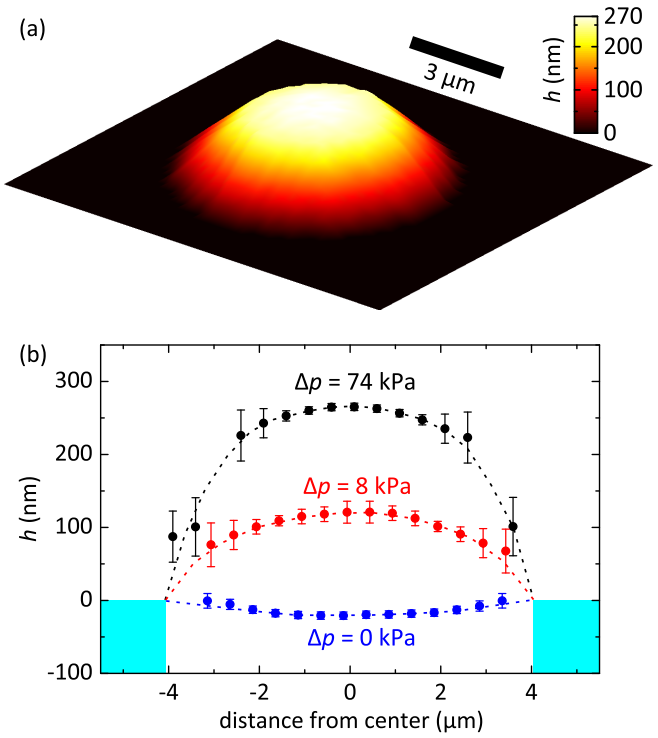

FIG. 5. Reconstruction of the blister topography. (a) Reconstructed three-dimensional image of the pressurized blister topography at $\Delta p = 74$ kPa. (b) Blister height profile recorded at various values of Δp. The error bars in (b) take into account the fact that it is not possible to give an accurate value of the height when the Raman intensity is approaching a local minimum [see Fig. 4(b)]. The dashed lines are guides to the eye.

$\Delta p \approx 30$ kPa. This feature also appears clearly in the theoretical calculation of the enhancement factor of the $2D$ mode near $h_{\text{tot}} \approx 580$ nm (i.e., $h \approx 185$ nm). This secondary maximum arises from the fact that the Raman enhancement factor is the product of an excitation term, with a quasiperiod of half the laser wavelength and a scattering term, with a larger quasiperiod of half the wavelength of the Raman scattered photons [40]. For Raman features at sufficiently large shifts (such as the $2D$-mode feature), this *beating* produces secondary maxima in the Raman enhancement factor. Conversely, a significant secondary maximum is neither expected nor observed for I_G in the height range investigated here. This observation further validates our experimental approach for the determination of the blister profile.

As an example, contour plots of I_G and of the corresponding blister height are presented as a function of Δp and r in Figs. 4(c) and 4(d). Similar data for I_{2D} and for another sample are shown in Supplemental Material [22]. We find that the heights deduced from I_G and I_{2D}, respectively, are very similar (see also Fig. 7). We are now able to investigate the blister topography in more detail. In Fig. 5(a), we show a three-dimensional image of the pressurized blister, reconstructed from the Raman map

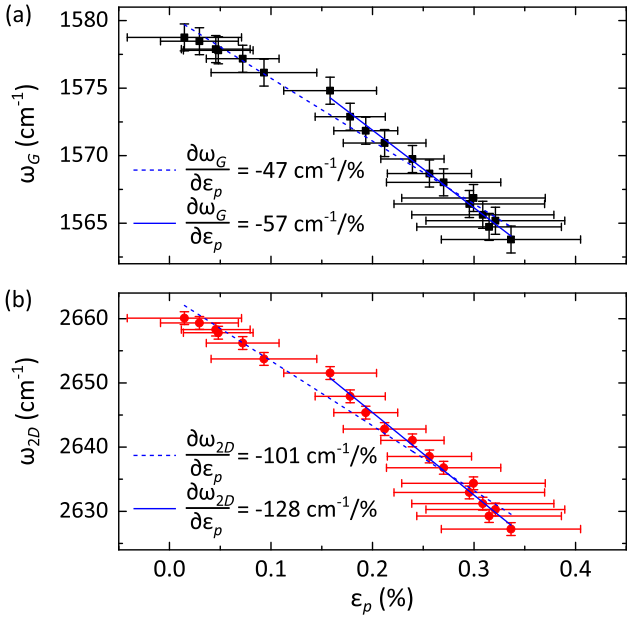

FIG. 6. Determination of the Grüneisen parameters. Evolution of the G-mode (a) and $2D$-mode (b) frequencies measured at the center of the sample shown in Fig. 1(a), as a function of the tensile strain ϵ_p induced by the uniform pressure load. The straight lines are linear fits.

of I_G shown in Fig. 3(a), by using the approach described above. Cross sections at different values of Δp are shown in Fig. 5(b). When approaching the border of the circular pit, the measured Raman intensities may be affected by contributions from the neighboring supported graphene. Therefore, the blister profile is linearly interpolated between $r = 3$ μm and $r = 4.1$ μm, where $h = 0$ nm.

V. DETERMINATION OF THE GRÜNEISEN PARAMETERS

Having determined the blister topography, we can now estimate an average tensile strain induced by the uniform pressure load $\epsilon_p = L/2a - 1$, where L is the length of the cross section of the pressurized graphene blister [see Fig. 5(b)]. We find that ϵ_p reaches values of up to $(0.33 \pm 0.07)\%$.

We can now correlate ϵ_p to the Raman frequencies ω_G and ω_{2D} measured at the center of the blister, as shown in Fig. 6. Over the range $\epsilon_p = 0\%$–0.33%, we observe roughly linear scalings with slopes $\partial\omega_G/\partial\epsilon_p = (-47 \pm 5)$ cm^{-1}/% strain and $\partial\omega_{2D}/\partial\epsilon_p = (-101 \pm 10)$ cm^{-1}/% strain, respectively. Nevertheless, in the limit of small deflections, a precise determination of ϵ_p remains challenging. Therefore, in the following, we consider the range $\epsilon_p = 0.1\%$–0.33%, for which ϵ_p can be estimated with sufficient accuracy. Within this range, we find slightly larger slopes of $\partial\omega_G/\partial\epsilon_p = (-57 \pm 5)$ cm^{-1}/% strain and $\partial\omega_{2D}/\partial\epsilon_p = (-128 \pm 10)$ cm^{-1}/% strain, respectively.

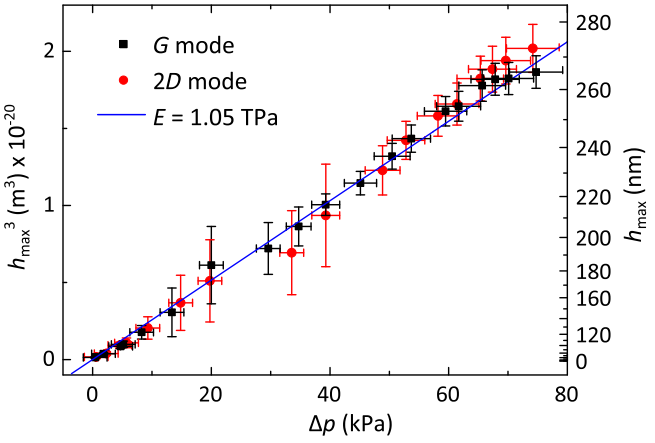

FIG. 7. Determination of the Young's modulus of graphene. Third power of the height of the graphene blister, h_{max}, measured at its center as a function of the pressure load. Data obtained from the measurement of the G- ($2D$-) mode integrated intensity are shown with black squares (red circles). The straight line is a linear fit, which allows one to deduce a Young's modulus of $E = (1.05 \pm 0.1)$ TPa.

These slopes allow us to estimate the Grüneisen parameters of the G and $2D$ modes under biaxial strain, as $\gamma_G = \frac{1}{2\omega_G^0}\frac{\partial\omega_G}{\partial\epsilon_p} = 1.8 \pm 0.2$ and $\gamma_{2D} = \frac{1}{2\omega_{2D}^0}\frac{\partial\omega_{2D}}{\partial\epsilon_p} = 2.4 \pm 0.2$, respectively, where ω_G^0 and ω_{2D}^0 are the G- and $2D$-mode frequencies, respectively, in pristine graphene.

VI. DETERMINATION OF THE YOUNG'S MODULUS OF GRAPHENE

We now consider the evolution of h_{max}, the height measured at the center of the blister, as a function of Δp. As demonstrated by Hencky in 1915 [42,43], the third power of deflection of a thin circular plate with negligible bending stiffness, i.e., a membrane, is expected to be proportional to Δp:

$$\Delta p = \frac{K(\nu)Et}{a^4} h_{max}^3, \tag{1}$$

where E is the Young's modulus, t is the thickness of the membrane ($t = 0.335$ nm for monolayer graphene), and $K(\nu)$ is a constant that depends on the Poisson ratio of the membrane. In addition, the volume of the blister V_B can be written as

$$V_B = C(\nu)\pi a^2 h_{max}, \tag{2}$$

where $C(\nu)$ is another constant that is directly related to $K(\nu)$ [42,43]. Similarly to the determination of ϵ_p, we also estimate V_B for each value of Δp (i.e., of h), and deduce an average $C(\nu) = 0.52 \pm 0.02$ (see Supplemental Material [22]). This value is very close to those previously suggested for monolayer graphene, by using $\nu \approx 0.16$, the

TABLE I. Comparison of our results with other works. Ratio of the shift rate of the 2*D* mode to that of the *G* mode under biaxial tensile strain, Grüneisen parameters for the *G*- and 2*D*-mode features, and Young's modulus of graphene determined in the present study. Our all-optical measurements are compared with experimental and theoretical values reported in the literature.

	Method	$\frac{\partial\omega_{2D}}{\partial\omega_G}$	γ_G	γ_{2D}	E (TPa)
This work	Raman	2.2 ± 0.1	1.8 ± 0.2	2.4 ± 0.2	1.05 ± 0.1
Graphene bubble [18]	Raman + AFM	2.45 ± 0.3	1.8 ± 0.2	2.6 ± 0.1	···
Suspended graphene [19]	Raman + simulation	2.2 ± 0.2	···	···	2.4 ± 0.4
Pristine graphene [27,44,45]	First principles	···	1.8–2.0	2.7 (Ref. [27])	···
Suspended graphene [3]	Nanoindentation	···	···	···	1.0 ± 0.1
Pristine graphene [46,47]	Molecular dynamics	···	···	···	1.0 ± 0.1

value of bulk graphite [4,5]. In these conditions, one expects $K(\nu) \approx 3$ [4,5,42,43].

In Fig. 7, we show the relationship between $h_{\max}^3$ and Δp. Both curves follow very similar linear scalings through the origin, in excellent agreement with Eq. (1). Using $K = 3.09$ [4,5] and $a = (4.1 \pm 0.1)$ μm, we determine the Young's modulus of monolayer graphene as $E = (1.05 \pm 0.1)$ TPa.

VII. DISCUSSION

A summary of our experimental results and a brief survey of relevant literature values are presented in Table I. Let us first consider the slope $\partial\omega_{2D}/\partial\omega_G$. Our value of 2.2 ± 0.1 is in good agreement with recent studies by Zabel *et al.* [18] on a graphene bubble and by Lee, Yoon, and Cheong [19] on suspended graphene. Interestingly, we demonstrate that the slope $\partial\omega_{2D}/\partial\omega_G$ is the same at the center of a pressurized blister, where strain is biaxial, and near its edges, where shear deformation (i.e., a uniaxial strain component) is present. We conclude that the value $\partial\omega_{2D}/\partial\omega_G = 2.2 \pm 0.1$, which also has been proposed by Lee *et al.* [31] for thermally annealed, supported graphene, seems to be universal for graphene, in the limit of moderate strains below 1%. As reported, larger uniaxial strains induce shear deformation and subsequent splittings of the Raman features, which strongly depend upon the polarization of the incoming and scattered phonons relative to the crystal orientation [20,27,28,32–34]. These factors complicate the determination of $\partial\omega_{2D}/\partial\omega_G$ and consequently of the Grüneisen parameters.

Under biaxial stress, the Grüneisen parameters are determined more reliably, since these are simply proportional to $\partial\omega_{2D}/\partial\omega_G$. The main challenge is then to determine the amount of strain with accuracy. Remarkably, our all-optical determination of ϵ_p, γ_G, and γ_{2D} agrees well with an estimation based on combined AFM and Raman measurements on a graphene bubble on a Si/SiO_2 substrate [18]. We also find good agreement with theoretical predictions [27,44,45]. Interestingly, we demonstrate that a direct determination of ϵ_p from the integrated intensity of the Raman features can be performed *in situ*, as a function of Δp. Although the lateral resolution of our approach is set by the diffraction limit, the measured heights can be estimated with precisions up to about 5 nm. Our approach also has the major advantage of being contactless and minimally invasive, as opposed to scanning probe techniques, such as AFM, where sample-tip interaction is known to lead to artifacts when probing the topography of the suspended membrane. In addition, our experimental setup is obviously easier and cheaper to implement than an *in situ* AFM setup, which would be an alternative way to probe the blister topography, as a function of a controllable pressure load with a better lateral resolution. In any event, we note that precise determinations of the Grüneisen parameters of graphene remain difficult, since these typically combine a local Raman measurement with an estimation of the amount of strain that is averaged over a much larger area. These experimental difficulties may, in part, explain the relatively large spread in the experimental values of γ_G and γ_{2D} reported in the literature.

Finally, our measurement of the Young's modulus of graphene matches the value of bulk graphite and is in excellent agreement with values obtained by using scanning probe techniques, such as nanoindentation [3] and AFM [4], as well as with molecular dynamics simulations [46,47]. Here, the Young's modulus is determined with accuracy by using a simple, all-optical, and minimally invasive approach. We note that Lee, Yoon, and Cheong have recently proposed a significantly larger value of E (see Table I and Ref. [19]). The latter estimate is obtained from a comparison of Raman scattering measurements with finite elements simulations [19]. We believe that this discrepancy is due to the fact that ϵ_p has been qualitatively estimated by using previously reported Raman measurements on uniaxially strained supported graphene [33]. This difference further highlights the interest of our approach, which allows a combined study of the topography and of the vibrational properties of suspended graphene, from a consistent set of measurements.

VIII. CONCLUSION

Using micro-Raman scattering spectroscopy, we have performed a constant N blister test on a suspended graphene membrane under a uniform pressure load. By analyzing the frequencies and the integrated intensities of the main Raman features of graphene, we reconstruct the

blister topography and deduce the Grüneisen parameters and the Young's modulus. Our analysis reveals that the intensity of the Raman features of a suspended graphene membrane can vary by one order of magnitude for pressure changes of only a few kPa [see also Fig. 4(a)]. Considering Eq. (1), the relative change in blister height will be particularly strong close to pressure equilibrium, i.e., for $\Delta p \approx 0$ kPa. This result suggests that typical fluctuations of the atmospheric pressure, as low as 1 kPa, could be sensed with accuracy, by using *graphene-based barometers*. Our approach can be implemented for all-optical adhesion studies, under larger pressure loads [4], and could directly be generalized to other two-dimensional materials, such as transition metal dichalcogenides [12].

More generally, we hope that our study may inspire original research efforts at the interface between electromechanics [48], optomechanics [14], and mechanical engineering. Indeed, the mechanical response of micro- and nanoresonators is highly sensitive to the stress conditions [8,13,49–53]. Our approach should permit one to measure the topography and strain distribution (including built-in strain [37,54]) of micro- and nanoresonators, in various environments, provided an interference pattern can develop. For instance, a readout of the mechanical resonance of few-layer graphene cantilevers through the frequency of the Raman features has recently been demonstrated [13]. A stimulating challenge is now to implement a real-time readout [55,56] of the mechanical resonances of nanosystems based on Raman scattering spectroscopy.

ACKNOWLEDGMENTS

We are grateful to Antoine Reserbat-Plantey and Guillaume Froehlicher for fruitful discussions. We thank Romain Bernard, Sabine Siegwald, and Hicham Majjad for help with sample fabrication in the STNano clean room facility and Bernard Doudin, Fabien Chevrier, and Arnaud Boulard for technical support. We acknowledge financial support from the Centre National de la Recherche Scientifique (CNRS), Université de Strasbourg, C'Nano GE, and the Agence Nationale de Recherche (ANR) under Grant No. QuandDoGra 12 JS10-00101.

[1] K. S. Novoselov, D. Jiang, F. Schedin, T. J. Booth, V. V. Khotkevich, S. V. Morozov, and A. K. Geim, Two-dimensional atomic crystals, Proc. Natl. Acad. Sci. U.S.A. **102**, 10451 (2005).

[2] A. H. Castro Neto, F. Guinea, N. M. R. Peres, K. S. Novoselov, and A. K. Geim, The electronic properties of graphene, Rev. Mod. Phys. **81**, 109 (2009).

[3] Changgu Lee, Xiaoding Wei, Jeffrey W. Kysar, and James Hone, Measurement of the elastic properties and intrinsic strength of monolayer graphene, Science **321**, 385 (2008).

[4] Steven P. Koenig, Narasimha G. Boddeti, Martin L. Dunn, and J. Scott Bunch, Ultrastrong adhesion of graphene membranes, Nat. Nanotechnol. **6**, 543 (2011).

[5] J. Scott Bunch, Scott S. Verbridge, Jonathan S. Alden, Arend M. van der Zande, Jeevak M. Parpia, Harold G. Craighead, and Paul L. McEuen, Impermeable atomic membranes from graphene sheets, Nano Lett. **8**, 2458 (2008).

[6] K. S. Novoselov, A. K. Geim, S. V. Morozov, D. Jiang, Y. Zhang, S. V. Dubonos, I. V. Grigorieva, and A. A. Firsov, Electric field effect in atomically thin carbon films, Science **306**, 666 (2004).

[7] J. S. Bunch, A. M. Van Der Zande, S. S. Verbridge, I. W. Frank, D. M. Tanenbaum, J. M. Parpia, H. G. Craighead, and P. L. McEuen, Electromechanical resonators from graphene sheets, Science **315**, 490 (2007).

[8] Changyao Chen, Sami Rosenblatt, Kirill I. Bolotin, William Kalb, Philip Kim, Ioannis Kymissis, Horst L. Stormer, Tony F. Heinz, and James Hone, Performance of monolayer graphene nanomechanical resonators with electrical readout, Nat. Nanotechnol. **4**, 861 (2009).

[9] Frank H. L. Koppens, Darrick E. Chang, and F. Javier Garcia de Abajo, Graphene plasmonics: A platform for strong lightmatter interactions, Nano Lett. **11**, 3370 (2011).

[10] R. R. Nair, P. Blake, A. N. Grigorenko, K. S. Novoselov, T. J. Booth, T. Stauber, N. M. R. Peres, and A. K. Geim, Fine structure constant defines visual transparency of graphene, Science **320**, 1308 (2008).

[11] Kin Fai Mak, Matthew Y. Sfeir, Yang Wu, Chun Hung Lui, James A. Misewich, and Tony F. Heinz, Measurement of the optical conductivity of graphene, Phys. Rev. Lett. **101**, 196405 (2008).

[12] Andres Castellanos-Gomez, Ronald van Leeuwen, Michele Buscema, Herre S. J. van der Zant, Gary A. Steele, and Warner J. Venstra, Single-layer MoS_2 mechanical resonators, Adv. Mater. **25**, 6719 (2013).

[13] Antoine Reserbat-Plantey, Laetitia Marty, Olivier Arcizet, Nedjma Bendiab, and Vincent Bouchiat, A local optical probe for measuring motion and stress in a nanoelectromechanical system, Nat. Nanotechnol. **7**, 151 (2012).

[14] Robert A. Barton, Isaac R. Storch, Vivekananda P. Adiga, Reyu Sakakibara, Benjamin R. Cipriany, B. Ilic, Si Ping Wang, Peijie Ong, Paul L. McEuen, Jeevak M. Parpia, and Harold G. Craighead, Photothermal self-oscillation and laser cooling of graphene optomechanical systems, Nano Lett. **12**, 4681 (2012).

[15] Steven P. Koenig, Luda Wang, John Pellegrino, and J. Scott Bunch, Selective molecular sieving through porous graphene, Nat. Nanotechnol. **7**, 728 (2012).

[16] U. Komaragiri, M. R. Begley, and J. G. Simmonds, The mechanical response of freestanding circular elastic films under point and pressure loads, J. Appl. Mech. **72**, 203 (2005).

[17] T. Georgiou, L. Britnell, P. Blake, R. V. Gorbachev, A. Gholinia, A. K. Geim, C. Casiraghi, and K. S. Novoselov, Graphene bubbles with controllable curvature, Appl. Phys. Lett. **99**, 093103 (2011).

[18] Jakob Zabel, Rahul R. Nair, Anna Ott, Thanasis Georgiou, Andre K. Geim, Kostya S. Novoselov, and Cinzia Casiraghi, Raman spectroscopy of graphene and bilayer under biaxial strain: Bubbles and balloons, Nano Lett. **12**, 617 (2012).

[19] Jae-Ung Lee, Duhee Yoon, and Hyeonsik Cheong, Estimation of Young's modulus of graphene by Raman spectroscopy, Nano Lett. **12**, 4444 (2012).

[20] Alexander L. Kitt, Zenan Qi, Sebastian Rémi, Harold S. Park, Anna K. Swan, and Bennett B. Goldberg, How graphene slides: Measurement and theory of strain-dependent frictional forces between graphene and SiO_2, Nano Lett. **13**, 2605 (2013).

[21] S. Berciaud, S. Ryu, L. E. Brus, and T. F. Heinz, Probing the intrinsic properties of exfoliated graphene: Raman spectroscopy of free-standing monolayers, Nano Lett. **9**, 346 (2009).

[22] See Supplemental Material at http://link.aps.org/supplemental/10.1103/PhysRevApplied.2.054008 for details on the determination of the pressure load, the determination of the blister height from the intensity of the 2*D*-mode feature, the influence of the laser-focusing conditions, polarization-resolved Raman measurements, data measured on other samples, and measurements on a concave graphene blister.

[23] L. M. Malard, M. A. Pimenta, G. Dresselhaus, and M. S. Dresselhaus, Raman spectroscopy in graphene, Phys. Rep. **473**, 51 (2009).

[24] Andrea C. Ferrari and Denis M. Basko, Raman spectroscopy as a versatile tool for studying the properties of graphene, Nat. Nanotechnol. **8**, 235 (2013).

[25] L. G. Cancado, A. Jorio, E. H. Martins Ferreira, F. Stavale, C. A. Achete, R. B. Capaz, M. V. O. Moutinho, A. Lombardo, T. S. Kulmala, and A. C. Ferrari, Quantifying defects in graphene via Raman spectroscopy at different excitation energies, Nano Lett. **11**, 3190 (2011).

[26] Axel Eckmann, Alexandre Felten, Artem Mishchenko, Liam Britnell, Ralph Krupke, Kostya S. Novoselov, and Cinzia Casiraghi, Probing the nature of defects in graphene by Raman spectroscopy, Nano Lett. **12**, 3925 (2012).

[27] T. M. G. Mohiuddin, A. Lombardo, R. R. Nair, A. Bonetti, G. Savini, R. Jalil, N. Bonini, D. M. Basko, C. Galiotis, N. Marzari, K. S. Novoselov, A. K. Geim, and A. C. Ferrari, Uniaxial strain in graphene by Raman spectroscopy: *G* peak splitting, Grüneisen parameters, and sample orientation, Phys. Rev. B **79**, 205433 (2009).

[28] M. Huang, H. Yan, C. Chen, D. Song, Tony F. Heinz, and J. Hone, Phonon softening and crystallographic orientation of strained graphene studied by Raman spectroscopy, Proc. Natl. Acad. Sci. U.S.A. **106**, 7304 (2009).

[29] Constanze Metzger, Sebastian Rémi, Mengkun Liu, Silvia V. Kusminskiy, Antonio H. Castro Neto, Anna K. Swan, and Bennett B. Goldberg, Biaxial strain in graphene adhered to shallow depressions, Nano Lett. **10**, 6 (2010).

[30] Fei Ding, Hengxing Ji, Yonghai Chen, Andreas Herklotz, Kathrin Dörr, Yongfeng Mei, Armando Rastelli, and Oliver G. Schmidt, Stretchable graphene: A close look at fundamental parameters through biaxial straining, Nano Lett. **10**, 3453 (2010).

[31] Ji Eun Lee, Gwanghyun Ahn, Jihye Shim, Young Sik Lee, and Sunmin Ryu, Optical separation of mechanical strain from charge doping in graphene, Nat. Commun. **3**, 1024 (2012).

[32] M. Huang, H. Yan, T. F. Heinz, and J. Hone, Probing strain-induced electronic structure change in graphene by Raman spectroscopy, Nano Lett. **10**, 4074 (2010).

[33] Duhee Yoon, Young-Woo Son, and Hyeonsik Cheong, Strain-dependent splitting of the double-resonance Raman scattering band in graphene, Phys. Rev. Lett. **106**, 155502 (2011).

[34] Otakar Frank, Marcel Mohr, Janina Maultzsch, Christian Thomsen, Ibtsam Riaz, Rashid Jalil, Kostya S. Novoselov, Georgia Tsoukleri, John Parthenios, Konstantinos Papagelis, Ladislav Kavan, and Costas Galiotis, Raman 2*D*-band splitting in graphene: Theory and experiment, ACS Nano **5**, 2231 (2011).

[35] S. Berciaud, X. Li, H. Htoon, L. E. Brus, S. K. Doorn, and T. F. Heinz, Intrinsic line shape of the Raman 2*D*-mode in freestanding graphene monolayers, Nano Lett. **13**, 3517 (2013).

[36] Sunmin Ryu, Li Liu, Stephane Berciaud, Young-Jun Yu, Haitao Liu, Philip Kim, George W. Flynn, and Louis E. Brus, Atmospheric oxygen binding and hole doping in deformed graphene on a SiO_2 substrate, Nano Lett. **10**, 4944 (2010).

[37] D. Metten, F. Federspiel, M. Romeo, and S. Berciaud, Probing built-in strain in freestanding graphene monolayers by Raman spectroscopy, Phys. Status Solidi B **250**, 2681 (2013).

[38] I. Calizo, A. A. Balandin, W. Bao, F. Miao, and C. N. Lau, Temperature dependence of the Raman spectra of graphene and graphene multilayers, Nano Lett. **7**, 2645 (2007).

[39] P. Blake, E. W. Hill, A. H. Castro Neto, K. S. Novoselov, D. Jiang, R. Yang, T. J. Booth, and A. K. Geim, Making graphene visible, Appl. Phys. Lett. **91**, 063124 (2007).

[40] Duhee Yoon, Hyerim Moon, Young-Woo Son, Jin Sik Choi, Bae Ho Park, Young Hun Cha, Young Dong Kim, and Hyeonsik Cheong, Interference effect on Raman spectrum of graphene on SiO_2/Si, Phys. Rev. B **80**, 125422 (2009).

[41] Antoine Reserbat-Plantey, Svetlana Klyatskaya, Valérie Reita, Laetitia Marty, Olivier Arcizet, Mario Ruben, Nedjma Bendiab, and Vincent Bouchiat, Time- and space-modulated Raman signals in graphene-based optical cavities, J. Opt. **15**, 114010 (2013).

[42] H. Hencky, Über den Spannungszustand in Kreisrunden Platten mit verschwindender Biegungssteifigkeit, Z. Angew. Math. Phys. **63**, 311 (1915).

[43] Kai-Tak Wan and Yiu-Wing Mai, Fracture mechanics of a new blister test with stable crack growth, Acta Metall. Mater. **43**, 4109 (1995).

[44] C. Thomsen, S. Reich, and P. Ordejón, *Ab initio* determination of the phonon deformation potentials of graphene, Phys. Rev. B **65**, 073403 (2002).

[45] Y. C. Cheng, Z. Y. Zhu, G. S. Huang, and U. Schwingenschlögl, Grüneisen parameter of the *G* mode of strained monolayer graphene, Phys. Rev. B **83**, 115449 (2011).

[46] Jin-Wu Jiang, Jian-Sheng Wang, and Baowen Li, Youngs modulus of graphene: A molecular dynamics study, Phys. Rev. B **80**, 113405 (2009).

[47] Xinjun Tan, Jian Wu, Kaiwang Zhang, Xiangyang Peng, Lizhong Sun, and Jianxin Zhong, Nanoindentation models and Young's modulus of monolayer graphene: A molecular dynamics study, Appl. Phys. Lett. **102**, 071908 (2013).

[48] M. L. Ekinci and K. L. Roukes, Nanoelectromechanical systems, Rev. Sci. Instrum. **76**, 061101 (2005).

[49] D. R. Southworth, R. A. Barton, S. S. Verbridge, B. Ilic, A. D. Fefferman, H. G. Craighead, and J. M. Parpia, Stress and silicon nitride: A crack in the universal dissipation of glasses, Phys. Rev. Lett. **102**, 225503 (2009).

[50] Vibhor Singh, Shamashis Sengupta, Hari S Solanki, Rohan Dhall, Adrien Allain, Sajal Dhara, Prita Pant, and Mandar M Deshmukh, Probing thermal expansion of graphene and modal dispersion at low-temperature using graphene nanoelectromechanical systems resonators, Nanotechnology **21**, 165204 (2010).

[51] P. Mohanty, D. A. Harrington, K. L. Ekinci, Y. T. Yang, M. J. Murphy, and M. L. Roukes, Intrinsic dissipation in high-frequency micromechanical resonators, Phys. Rev. B **66**, 085416 (2002).

[52] Bogdan Bercu, Xin Xu, Laurent Monts, and Panagiota Morfouli, Characterization of mechanical stress on nanostructures for nems applications by ultra-thin membrane and self-suspension techniques, Microelectron. Eng. **86**, 1303 (2009).

[53] M. Bauer, A. M. Gigler, C. Richter, and R. W. Stark, Visualizing stress in silicon micro cantilevers using scanning confocal Raman spectroscopy, Microelectron. Eng. **85**, 1443 (2008).

[54] L. A. Starman, Jr., J. A. Lott, M. S. Amer, W. D. Cowan, and J. D. Busbee, Stress characterization of mems microbridges by micro-Raman spectroscopy, Sens. Actuators A **104**, 107 (2003).

[55] Chenyang Xue, Lina Zheng, Wendong Zhang, Binzhen Zhang, and Aoqun Jian, A dynamic stress analyzer for microelectromechanical systems (MEMS) based on Raman spectroscopy, J. Raman Spectrosc. **38**, 467 (2007).

[56] J. W. Pomeroy, P. Gkotsis, Meiling Zhu, G. Leighton, P. Kirby, and M. Kuball, Dynamic operational stress measurement of MEMS using time-resolved Raman spectroscopy, J. Microelectromech. Syst. **17**, 1315 (2008).